Observations of Superinertial and Near-Inertial Wind-driven Flow*

DANIEL L. RUDNICK

School of Oceanography, University of Washington, Seattle, Washington

ROBERT A. WELLER

Woods Hole Oceanographic Institution, Woods Hole, Massachusetts

ABSTRACT

The superinertial and near-inertial wind-driven flow in the western North Atlantic is examined using data from two recent experiments. The Frontal Air–Sea Interaction Experiment (FASINEX) took place at 27°N, 70°W during 1986. The Long-Term Upper-Ocean Study (LOTUS) took place at 34°N, 70°W during 1982. Each experiment included moored measurements of meteorological variables that allowed estimation of the wind stress and oceanic currents. The directly wind-driven flow is isolated from other sources of variability, such as internal waves and mooring motion, using a transfer function between geocentric acceleration and wind stress. The transfer function is examined in rotary spectral bands bounded by periods of 36 and 12 h, and 12 and 2 h. For surface-moored observations, wind-driven mooring motion is found to cause a response that extends at least to 1000 m (much deeper than the frictional layer of direct wind forcing). Once this artifact is removed, the directly wind-driven flow is identified. This response is found to rotate to the left (right) for clockwise (counterclockwise) rotating superinertial wind stress, in agreement with the solution of the time-dependent Ekman spiral. When vertically integrated the Ekman transport relation is satisfied, indicating that all of the wind-driven flow has been isolated.

1. Introduction

Two recent papers have examined subinertial wind-driven flow in the western North Atlantic. Price et al. (1987, hereafter P87) used data from the Long-Term Upper Ocean Study (LOTUS) that took place at 34°N, 70°W during 1982, and Weller et al. (1991, hereafter W91) used data from the Frontal Air–Sea Interaction Experiment (FASINEX) that took place at 27°N, 70°W during 1986. In each case, the directly wind-driven flow was identified and found to agree with the Ekman transport relation. In addition, the wind-driven flow turned to the right with increasing depth as expected for a subinertial Ekman spiral. In this paper we investigate the wind-driven flow at superinertial and near-inertial frequencies; a topic that was not addressed in P87 or W91.

The first theory of wind-driven flow on a rotating earth was given by Ekman (1905), who postulated a balance between the Coriolis force and turbulent stress parameterized with a constant eddy viscosity. The so-lution for a steady wind stress was found to spiral to the right in the Northern Hemisphere and decay as a function of depth. It is a simple matter to add time dependence and to investigate the response to a wind stress rotating at a particular frequency. The resulting current spirals to the left (right) with depth for clockwise (counterclockwise) rotating superinertial frequencies.

Observational confirmation of this behavior has been difficult to obtain because the signal-to-noise ratio is low. The signal in this case is the frictional wind-driven flow, while the noise may be due to geostrophic flow at subinertial frequencies, internal waves at superinertial frequencies, and especially free inertial motions. These sources of noise are usually more energetic than the directly wind-driven signal. Another complicating factor is that observations are generally made from moorings, which may move in response to wind and currents and are far from stable platforms. Because of the low signal to noise ratio, many degrees of freedom are needed to isolate the wind-driven signal. It is only within the last decade that sufficiently long time series of wind stress and current have been collected to overcome the signal-to-noise problem.

We review the solution of a time-dependent Ekman spiral in section 2. The data from FASINEX and LOTUS used to examine the wind-driven flow are described in section 3. The transfer function approach

(Davis et al. 1981, hereafter D81; W91) to isolating the wind-driven response is presented in section 4. The results and their implications are discussed in section 5.

2. Theoretical considerations

A theoretical discussion of wind-driven currents must begin with the Ekman spiral. Ekman (1905) assumed a balance between the Coriolis force and turbulent friction to derive the oceanic response to a steady wind stress. The resulting current turns to the right (in the Northern Hemisphere) and decays as a function of depth, where the e-folding depth is $(2\nu/f)^{1/2}$, ν is the eddy viscosity, and f is the Coriolis parameter.

We review the addition of time dependence by considering the linear momentum equation

$$\frac{\partial u}{\partial t} + ifu = \frac{1}{\rho}\frac{\partial \tau}{\partial z}, \tag{1}$$

where ρ is the density (assumed constant), and u and τ are velocity and turbulent stress written as complex variables (for instance, u is equal to the eastward velocity plus i times the northward velocity). The pressure gradient has been ignored on the assumption that horizontal gradients are negligible. To get a solution to (1) a parameterization for turbulent stress must be adopted. A particularly simple choice, and the one used by Ekman (1905), is that the stress can be parameterized with a constant eddy viscosity ν:

$$\tau = \rho\nu\frac{\partial u}{\partial z}. \tag{2}$$

Using (2) in (1), and assuming a solution of the form $u = Ue^{i\omega t}$, we find

$$U = u_0 \exp\left[(1 \pm i)\left(\frac{|f + \omega|}{2\nu}\right)^{1/2}z\right], \tag{3}$$

where u_0 is the velocity at the surface and we have taken z to be positive upward. In the argument of the exponential, the imaginary part is positive for $f + \omega > 0$ and negative for $f + \omega < 0$. Using the stress boundary condition,

$$u_0 = \frac{\tau_0(1 \mp i)}{\rho\sqrt{2\nu\,|f + \omega|}}, \tag{4}$$

where τ_0 is the stress at the surface. Here the imaginary part is negative for $f + \omega > 0$ and positive for $f + \omega < 0$. Choosing $\omega = 0$ yields the steady Ekman spiral. The e-folding depth and the rotation of the current with depth vary as a function of the driving frequency ω. For superinertial, positive (counterclockwise rotating) frequency, $\omega > f$, the surface current is 45° to the right of the wind and the current rotates to the right with depth. For superinertial, negative (clockwise rotating) frequency $\omega < -f$, the surface current is 45°

to the left of the wind and the current rotates to the left with depth. The e-folding depth increases as ω approaches $-f$, where there is a resonance with free inertial currents.

It is convenient to examine oceanic response to wind in terms of the geocentric acceleration,

$$A \equiv \frac{\partial u}{\partial t} + ifu, \tag{5}$$

which effectively filters free inertial motions and thus eliminates the resonance for a driving frequency of $-f$. The surface value of geocentric acceleration is then

$$A_0 = (1 \pm i)\frac{\tau_0}{\rho}\left(\frac{|f + \omega|}{2\nu}\right)^{1/2}. \tag{6}$$

For positive (negative) superinertial frequency the surface geocentric acceleration is 45° to the left (right) of the wind. In addition, A approaches zero as ω approaches $-f$. The turning and decay of A with depth is identical to that of u.

3. Data

We use data obtained during a pair of experiments, FASINEX and LOTUS, that took place in the western North Atlantic. Currents were measured using both Vector Averaging Current Meters (VACMs) and Vector Measuring Current Meters (VMCMs). In each case, meteorological instrumentation aboard surface buoys allowed estimation of the wind stress. Details of the instrumentation and data in each experiment are given in this section.

From FASINEX (Weller et al. 1990a; Weller et al. 1990b), we use 102-day-long hourly time series extending from February through May 1986, gathered from five surface moorings. The 102-day time period was the longest common interval of good data on all five moorings. Each mooring had meteorological instrumentation on the surface buoy and current meters

TABLE 1. A summary of FASINEX data used in this study. The locations of good 102-day long time series of currents are marked x. Blanks indicate instruments that failed to return good time series. There were no current meters at 1000 or 4000 m on moorings F2, F6, and F10.

Depth (m)	Mooring				
	F2	F4	F6	F8	F10
10	x	x	x	x	x
20	x		x	x	x
30	x	x	x	x	x
40	x	x		x	x
80	x	x	x	x	
120		x			
160	x	x	x	x	x
700	x	x	x	x	
1000		x		x	
4000		x		x	

at 10, 20, 30, 40, 80, 120, 160, and 700 m. In addition, two of the moorings had current meters at 1000 and 4000 m. Some of the current meters had records shorter than 102 days; the data used here are summarized in Table 1. The moorings were deployed in a triangle pattern with moorings F2, F6, F4, and F8 along a southeastward line of approximately 53-km length, and mooring F10 placed 28 km to the northeast of this line.

From LOTUS (Briscoe and Weller 1984), we use 160-day long hourly time series extending from May through October 1982, gathered from a surface and a subsurface mooring. The surface mooring had meteorological instrumentation and current meters at 5, 10, 15, 20, 25, 35, 50, 65, 75, and 100 m. The subsurface mooring had current meters at 129, 178, 228, 278, 328, 775, 1024, 1521, and 4007 m. The moorings were located within about 7 km of each other and we expect no appreciable difference in the wind forcing over this

FIG. 2. Rotary autospectra of geocentric acceleration at 10 m multiplied by density for (a) FASINEX mooring F2 and (b) LOTUS. The solid line is the spectrum for positive frequencies, and the dashed line is for negative frequencies; 95% confidence intervals are indicated below the spectra.
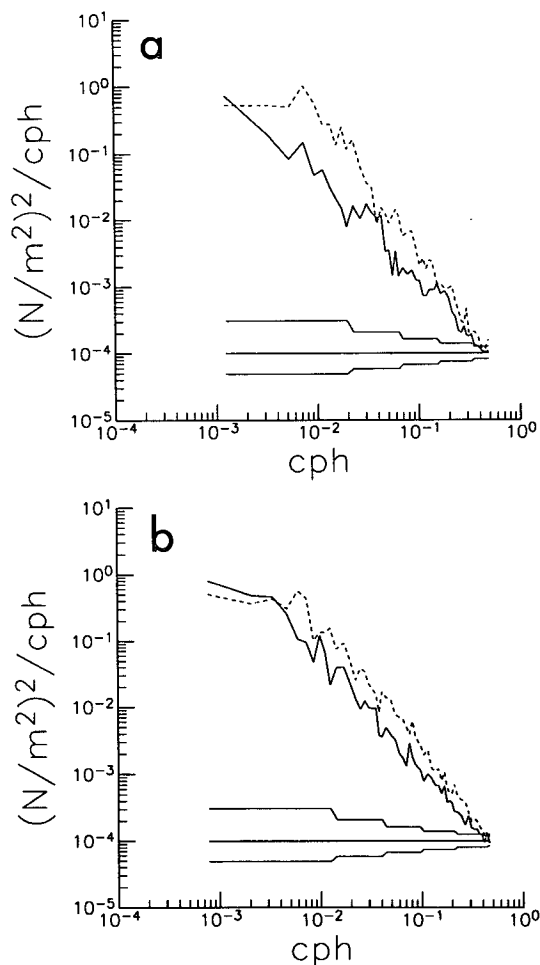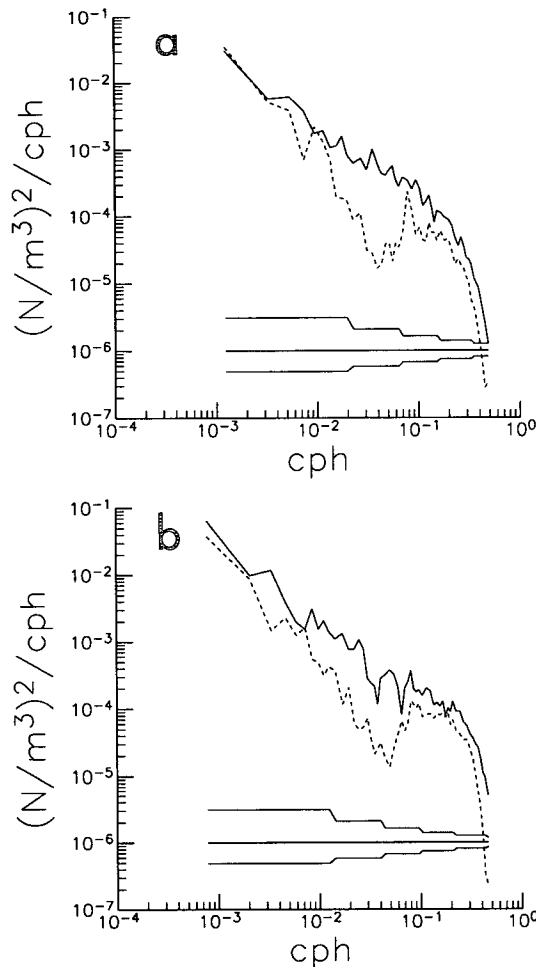

FIG. 1. Rotary autospectra of wind stress for (a) FASINEX mooring F2 and (b) LOTUS. The spectrum for positive (counterclockwise rotating) frequencies is indicated by the solid line, and the spectrum for negative (clockwise rotating) frequencies is the dashed line; 95% confidence intervals are indicated below the spectra.

range. The current meter at 5 m produced a short record of only 90 days.

4. Analysis and results

The goal of the analysis is to isolate the directly wind-forced flow. Momentum is transported to the upper ocean through the wind stress. Direct measurements of wind stress were not available, and bulk parameterizations were used to estimate the wind stress from the measurable quantities: wind velocity and sea surface and air temperatures (Large and Pond 1981; Weller et al. 1990a). Spectra of wind stress in LOTUS and FASINEX are similar (Fig. 1). For frequencies lower than about 0.02 cycles per hour (cph) during FASINEX, spectral levels at negative (clockwise rotating) frequencies are significantly higher than those at positive (counterclockwise rotating) frequencies. The difference

in spectral levels is due to a series of weather systems moving eastward consistently to the north of the FA-SINEX array. At higher frequencies (the subject of this study) there is a slight tendency for negative frequencies to be more energetic than positive frequencies, although the difference is not significant.

The geocentric acceleration (5) is estimated from the current meter data using a centered difference for the time derivative. Rotary spectra of the geocentric acceleration, multiplied by density, from LOTUS and FASINEX are shown in Fig. 2. Spectral levels are similar during the two experiments. A spectral well occurs near a frequency of $-f$, because free inertial motions have zero geocentric acceleration. The use of geocentric acceleration instead of current improves the signal to noise ratio by explicitly filtering free inertial motions.

Based on the momentum equation, a transfer function between geocentric acceleration and wind stress is used to identify the wind-driven flow. Our model of wind-driven flow is

$$\hat{A} = a \frac{\tau_0}{\rho}, \qquad (7)$$

where $\hat{A}$ is the geocentric acceleration that is coherent with the wind stress τ_0, and a is the transfer function in units of inverse meters. The transfer function is calculated as a function of frequency ω for each instrument by minimizing the mean-square difference between the modeled and measured geocentric acceleration. The result is

$$a = \rho \frac{\langle \tau_0^* \hat{A} \rangle}{\langle \tau_0^* \tau_0 \rangle}, \qquad (8)$$

where the angle brackets represent an ensemble average (in this case over frequency bands) and the asterisk means complex conjugate. For this model to be successful in isolating the frictional wind-driven flow, the momentum balance must be linear as supposed in (1). Also, the pressure gradient must be incoherent with the wind stress, or else the transfer function will include components that are indirectly driven by the wind through pressure gradients. The success of the model is determined a posteriori by examining the transport.

The transfer function is calculated for each instrument in FASINEX and LOTUS in positive and negative frequency bands bounded by 0.028 and 0.083 cph (the near-inertial band, periods between 36 and 12 h), and 0.083 and 0.5 cph (the superinertial band,
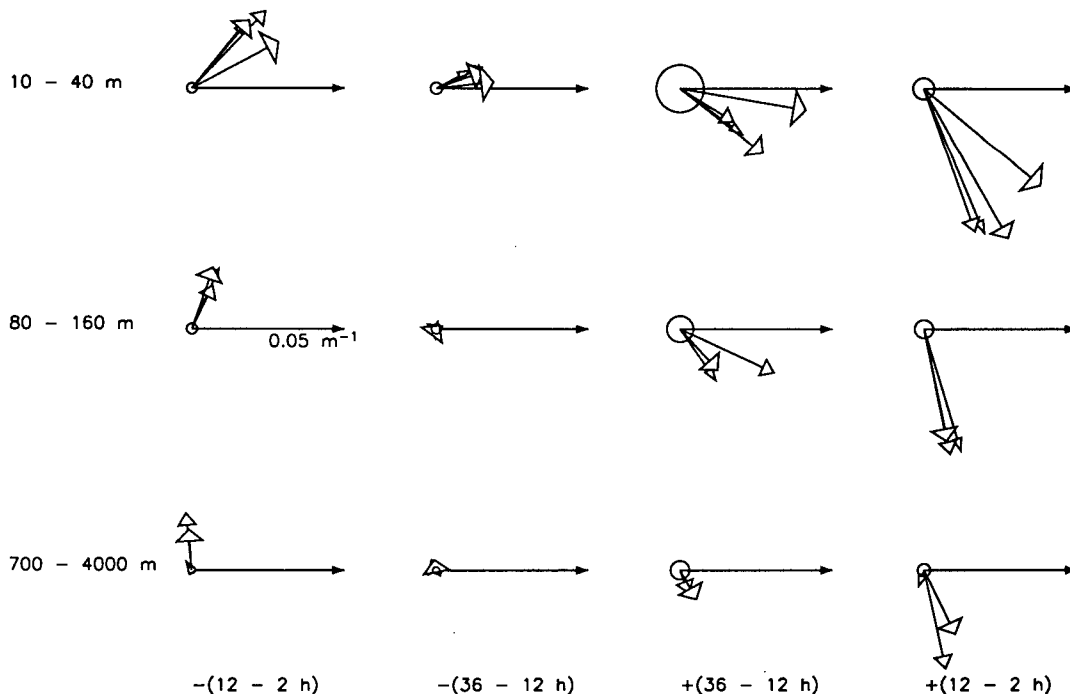

FIG. 3. The transfer function (8) for FASINEX. The four columns of hodographs show the transfer function in four frequency bands: positive and negative 0.028–0.083 cph (36–12-h periods), and 0.083–0.5 cph (12–2-h periods). The rows are groups of transfer functions at neighboring depths. The upper row includes 10, 20, 30, and 40 m (the frictional layer); the center row includes 80, 120, and 160 m (the seasonal thermocline); and the bottom row includes 700, 1000, and 4000 m (the interior). The solid-ended arrows indicate the direction of the real axis and the scale 0.05 m⁻¹. The open-ended arrows are the transfer functions where the heads become smaller with depth in each group. The real axis indicates the wind direction, and the transfer function is the response to the wind. The random error for one of the estimates in each group is indicated by the circle centered at the base of the arrows. In the frictional layer the error at 10 m is shown; in the seasonal thermocline the error is for 160 m; and in the interior the error is for 700 m.

periods between 12 and 2 h). These particular bands were chosen to separate the behavior at near- and superinertial frequencies and to get sufficient degrees of freedom. The inertial periods for FASINEX and LOTUS are 26.4 and 21.5 h, respectively, so the negative 36–12-h band brackets the inertial frequency. The FASINEX results are averaged over the five moorings. The transfer function in each of the four frequency bands is shown in four columns (Figs. 3 and 4). The transfer function is plotted in groups of hodographs, with the solid-ended vectors indicating the real axis and the open-ended vectors being the transfer function at neighboring depths. In each group, the vectors' head width decreases with depth. One may think of the real axis as the direction of the wind and the transfer function as the response to the wind. For FASINEX, the upper group includes 10, 20, 30, and 40 m; the middle

group 80, 120, and 160 m; and the lower group 700, 1000, and 4000 m. For LOTUS, the upper group in each band includes 5, 10, 15, 20, and 25 m, and the next group 35, 50, 65, 75, and 100 m. All of these instruments are from the surface mooring. The lower two groups are from the subsurface mooring: 129, 178, 228, 278, and 328 m; and 775, 1024, 1521, and 4007 m. In general, we may consider the upper group in each experiment to be in the frictional layer, the middle group(s) to be in the seasonal thermocline, and the lower group to be in the interior. Random errors are indicated by the circles and are calculated as in Bendat and Piersol (1986).

The response is clearly surface intensified in all frequency bands, as might be reasonably expected. More surprising, however, is the deep response, extending down to 1000 m, during FASINEX. This response is
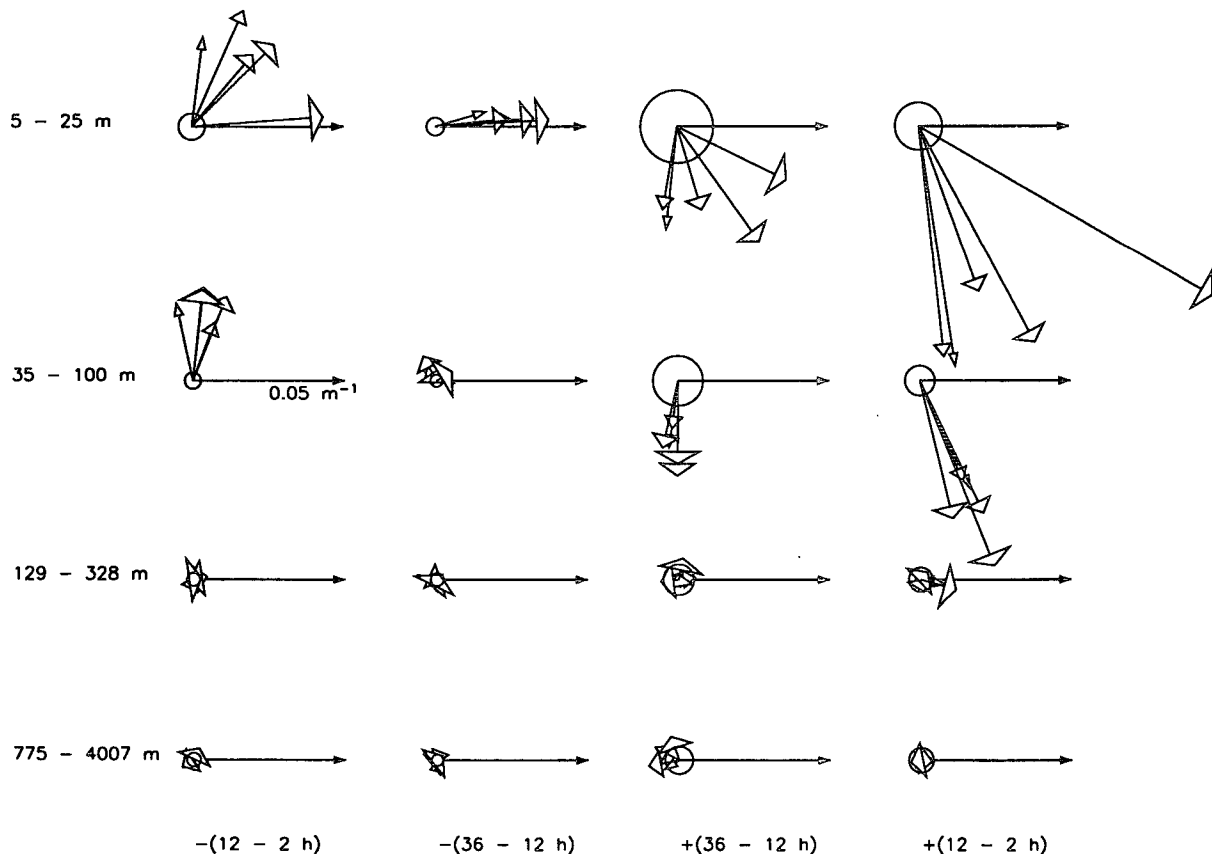

FIG. 4. The transfer function (8) for LOTUS. The four columns of hodographs show the transfer function in four frequency bands: positive and negative 0.028–0.083 cph (36–12-h periods), and 0.083–0.5 cph (12–2-h periods). The rows are groups of transfer functions at neighboring depths. The upper row includes 5, 10, 15, 20, and 25 m (the frictional layer); the second row includes 35, 50, 65, 75, and 100 m (the seasonal thermocline, surface mooring); the third row includes 129, 178, 228, 278, and 328 m (the seasonal thermocline, subsurface mooring); and the bottom row includes 775, 1024, 1521, and 4007 m (the interior). The solid-ended arrows indicate the direction of the real axis and the scale 0.05 m^{-1}. The open-ended arrows are the transfer functions where the heads become smaller with depth in each group. The real axis indicates the wind direction, and the transfer function is the response to the wind. The random error for one of the estimates in each group is indicated by the circle centered at the base of the arrows. In the frictional layer the error at 10 m is shown; in the seasonal thermocline, surface mooring, the error is for 100 m; in the seasonal thermocline, subsurface mooring, the error is for 178 m; and in the interior the error is for 775 m.

strongest in the superinertial bands where it is to the right of the wind for positive and to the left for negative frequencies, and weakest in the clockwise rotating near-inertial band. This is not predicted by theory, as one would not expect vertically propagating internal waves to maintain coherence with the local wind (Philander 1978). This response can be seen as well in the LOTUS data down to 100 m; however, it disappears at 129 m. Since the observations down to 100 m are from the surface mooring and the observations at 129 m and deeper are from the subsurface mooring, we suspect that this response is due to mooring motion as the surface buoy is pushed around by the wind.

The mooring-induced response can be understood by supposing that the measured current is the true current less the mooring motion,

$$u = u_T - u_M,$$ (9)

where u_T is the true current and u_M is the mooring motion. Decomposing the mooring motion into a part coherent with the wind and a part incoherent with the wind,

$$u_M = c\tau_0 + u'_M,$$ (10)

where c is the transfer function between mooring motion and wind stress. Mooring dynamics determine c as a function of frequency and depth. It is reasonable to assume that the mooring motion tends to be in phase with the wind so that c is mostly real. Using the definition (5) and substituting (9) and (10) into (8) yields the measured transfer function,

$$a = a_T - i(\omega + f)c,$$ (11)

where a_T is the true transfer function, which is presumably confined to the frictional layer in the upper ocean. For real c, the model predicts mooring motion–induced negative (positive) imaginary response at positive (negative) superinertial frequencies as observed. The model also suggests that the bogus response should be largest for the highest positive frequencies and should vanish at $\omega = -f$. The observed deep mooring–induced response is indeed not significantly different from zero in the negative near-inertial band; that is, inertial mooring motion is filtered as effectively as free inertial motion. The response decays with depth since the mooring anchor is fixed. A better confirmation that this response is mooring induced requires good measurements of the horizontal motion of each instrument on the mooring. While buoy positions during FASI-NEX were recorded via ARGOS, these data are unreliable at high frequencies (Weller et al. 1990b).

To examine the frictional wind-driven flow, the bogus mooring-induced response must be removed. This removal formally requires knowledge of c as a function of frequency and depth. We assume that at a reference depth z_r the flow is due only to mooring motion and that the mooring-induced response is uniform from z_r to the surface. The upper 100 m of the moorings were

observed to be hanging nearly vertically during FA-SINEX (Weller et al. 1990b), supporting the assumption that the mooring-induced response is uniform above z_r. The transfer function a_r at z_r is then subtracted from shallower values to isolate the frictional response,

$$\hat{A}_w = (a - a_r)\frac{\tau_0}{\rho}.$$ (12)

Our ability to isolate the frictional flow may be tested by substituting the modeled geocentric acceleration (12) into (1) and integrating vertically,

$$\int_{z_r}^{0} (a - a_r)dz = 1.$$ (13)

If this relation, which is equivalent to the Ekman transport relation, is satisfied, then we conclude that we have isolated all of the wind-driven flow. The preceding integral is estimated using the trapezoidal rule. Richman et al. (1987) point out that near-surface shears may be quite large. Extrapolation to the surface is accomplished by assuming that the vertical gradient between the upper two estimates of a continues to the surface.

Estimates of transport for FASINEX are in good agreement with theory (Fig. 5). The time-mean mixed-layer depth, as determined by a 0.1°C decrease from the temperature at 1 m, is 44 m; we choose an 80-m reference depth since this is the shallowest instrument below the mean mixed-layer depth. In every frequency band the integrated transfer function is within twice the random error (roughly 95% confidence limits) of the theoretical value of 1. Furthermore, the frictional wind-driven response spirals with depth to the left for negative frequencies and to the right for positive frequencies. Although this spiral is not perfectly smooth, it is evident nonetheless. The shallowest measured response at 10 m is to the right of the wind in the negative superinertial band and to the left of the wind in the positive bands as might be expected from the solution (6).

Transport estimates for LOTUS (Fig. 6) are not as good in the sense that (13) is not satisfied as well as for FASINEX. The mean mixed-layer depth for LO-TUS is 22 m, and a 35-m reference depth is chosen to be well beneath the depth of the mean mixed layer. The transport in the positive near-inertial band is not significantly different from zero. However, there is a tendency for the response to be in the right direction even though it is too small. A leftward-turning spiral is apparent in the negative superinertial band, while essentially no turning can be seen in the negative near-inertial band. The theoretical Ekman spiral penetrates deeper and turns slower with depth as the frequency approaches $-f$, so perhaps this behavior is not surprising. For positive frequencies, the turning is in the theoretical sense from 5 to 10 m but is confused deeper. The shallowest response in all but the negative near-
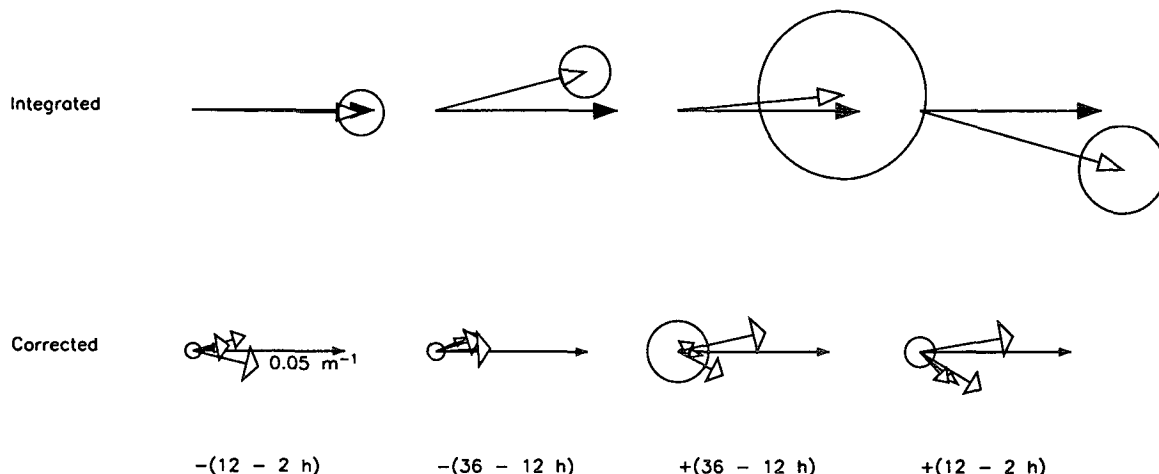
FIG. 5. The FASINEX transfer function corrected for mooring motion [Eq. (12), bottom row] and vertically integrated [Eq. (13), top row] for each of the four frequency bands. In the bottom row, the solid-ended arrows indicate the direction of the real axis and the scale 0.05 m⁻¹, and the open-ended arrows are the corrected transfer functions for depths 10, 20, 30, and 40 m. The circle centered at the base of the arrows indicates the random error for the 10-m estimate. In the top row, the solid-ended arrows have length 1 and the open-ended arrows are the integrated, corrected transfer functions. The circle centered on the tip of the open-ended arrow is the random error in the integrated, corrected transfer function.

inertial band shows the same directional relation to the wind as expected from theory and as seen in the FA-SINEX data. The results are not as clear in the LOTUS data, probably because there are fewer degrees of freedom. The FASINEX results are averaged over as many as five moorings, while there is only one estimate at each depth for LOTUS.

Random errors in all quantities are noticeably smaller for negative frequency bands, especially in the near-inertial band. This is a reflection of higher signal

to noise ratios in these bands because, first, the wind stress is more energetic at negative frequencies and, second, the noise in the near-inertial band is filtered by the use of geocentric acceleration. The dominance of clockwise over counterclockwise wind stress is a feature of these data that will not, in general, be found elsewhere in the ocean. However, the filtering of near-inertial noise is a consequence of the analysis and should be seen in other datasets.
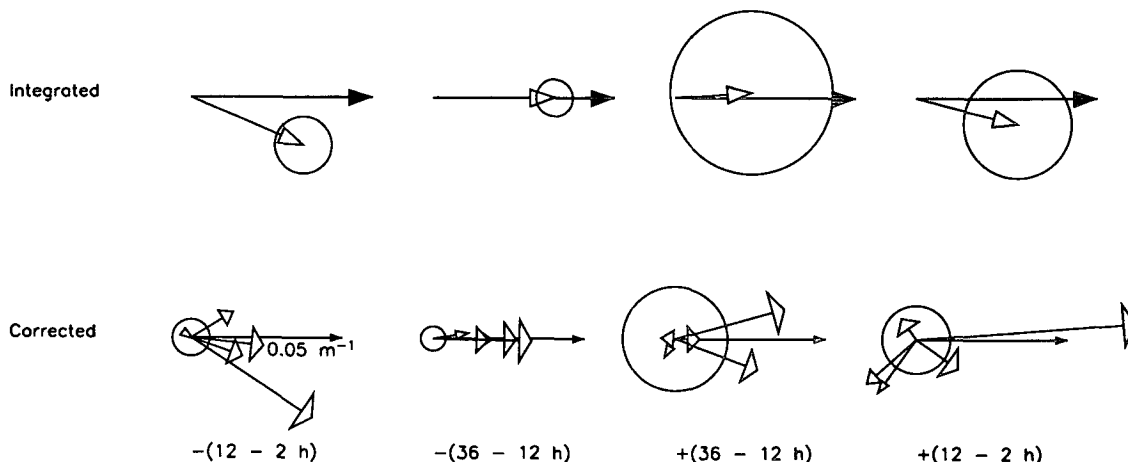
The wind-driven response is smaller than expected

FIG. 6. The LOTUS transfer function corrected for mooring motion [Eq. (12), bottom row] and vertically integrated [Eq. (13), top row] for each of the four frequency bands. In the bottom row, the solid-ended arrows indicate the direction of the real axis and the scale 0.05 m⁻¹, and the open-ended arrows are the corrected transfer functions for depths 5, 10, 15, 20, and 25 m. The circle centered at the base of the arrows indicates the random error for the 10-m estimate. In the top row, the solid-ended arrows are pure real of length 1 and the open-ended arrows are the integrated, corrected transfer functions. The circle centered on the tip of the open-ended arrow is the random error in the integrated, corrected transfer function.

for both FASINEX and LOTUS (with the exception of the positive superinertial band for FASINEX). This can be partially rationalized by the overresponse of the cup anemometers used to measure wind. Wind measurements were 6% high during FASINEX, resulting in stress estimates 12% high (Weller et al. 1990a). Thus, the transfer functions shown here should be underestimates of the true transfer functions. Increasing the magnitude of the transfer functions by 12% would bring the calculated transport of all but the FASINEX positive superinertial band into closer agreement with theory. This, does not account for all of the underresponse during LOTUS, however. Deeper reference depths yield transports in marginally better agreement with theory for both FASINEX and LOTUS negative near-inertial bands. The Ekman spiral's penetration depth approaches infinity as ω approaches $-f$, and if z_r is too shallow, some of the wind-driven flow may be missed.

Nonlinear interactions between the wind-driven flow and the underlying, presumably geostrophic flow may affect the transfer function. By specifying a linear momentum balance, these interactions are a component of the noise in our system. However, the nonlinear effects appear to average out over the course of the deployments since the transports tend to agree with linear theory. The momentum equations for the wind-driven component in the presence of a background flow field can be written (Weller 1982):

$$\frac{\partial u}{\partial t} + \frac{\partial U}{\partial x} u + \left(\frac{\partial U}{\partial y} - f\right)v = \frac{\partial \tau_x}{\partial z} \quad (14a)$$

$$\frac{\partial v}{\partial t} + \left(\frac{\partial V}{\partial x} + f\right)u + \frac{\partial V}{\partial y} v = \frac{\partial \tau_y}{\partial z}, \quad (14b)$$

where (u, v) is the wind-driven flow and (U, V) is the background flow. These equations are derived by assuming that the wind-driven component has negligible horizontal gradient and therefore vanishing vertical velocity, and that the divergence δ in the background flow is small compared to the vorticity ζ, so vertical advection by the background flow is negligible. A result of these equations is that the effective inertial frequency is shifted by $\zeta/2$. This shift should be most noticeable in the negative near-inertial band of the transfer function where $|\omega + f|$ is a minimum. Positive (negative) divergence causes exponential decay (growth) with time scale $(\delta/2)^{-1}$. Because the divergence in nearly geostrophic flows is small compared to the vorticity, this effect is relatively unimportant.

The FASINEX array provides an opportunity to calculate the horizontal gradients in (14) and to include the nonlinear effects in the transfer function. The horizontal gradients are calculated as an average over the array using the time mean and the first three empirical orthogonal functions (Eriksen et al. 1991, Fig. 12). The use of the empirical orthogonal functions filters out unresolved small-horizontal-scale variability, so the estimated gradients reflect only the resolved array scale (Rudnick and Davis 1988). The time-mean vorticity

over the deployment is $-0.06f$, indicating a very small mean 3% reduction in inertial frequency. FASINEX is characterized by the passage of several strong fronts with vorticities approaching $f/3$, and the wind-driven flow during the frontal passages should be affected. Peak divergences are approximately one-fifth the vorticity, so divergence is small relative to vorticity, as expected.

Using the lhs of (14) in place of the geocentric acceleration, the transfer function is calculated. The largest difference from the linear transfer function is in the negative near-inertial band where it is barely significant (Fig. 7). The tendency is to bring the transport into closer agreement with theory. The wind-driven flow is, at least slightly, affected by gradients in the background flow field. Although the interaction is small when averaged over the entire deployment, the effect may be quite important when the vorticity peaks during frontal passages.

5. Discussion

The high-frequency frictional wind-driven flow has been isolated using data from two experiments in the western North Atlantic. The flow spirals to the left in response to a clockwise-rotating superinertial wind stress and to the right in response to a counterclockwise wind stress. This behavior is in agreement with the time-dependent Ekman spiral. The Ekman transport relation is satisfied reasonably well for the FASINEX data, while calculated transport is somewhat low for LOTUS. These results as well as the spirals observed at subinertial frequencies by D81, P87, and W91 show that directly wind-driven flow can be observed at all frequencies.
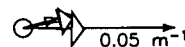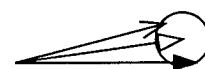
$-(36 - 12\ h)$

FIG. 7. The FASINEX transfer function including nonlinear effects [as in Eq. (14)] for the negative 36–12-h band. The lower hodograph is corrected for mooring motion. In the upper hodograph, the solid arrow is pure real of length 1 and the open arrow is the integrated, corrected transfer function including nonlinear effects. The circle centered on the tip of the open-ended arrow is the random error in the integrated, corrected transfer function. The integrated linear transfer function (from Fig. 5) is drawn for reference as the arrow with the stick head.

These results do not necessarily imply that it is appropriate to model turbulent friction with a constant eddy viscosity. The proper implication is that turbulent transport of momentum is a function of shear, since some sort of dependence on shear is required for there to be spiraling in the wind-driven flow. Just what the functional form of turbulent friction might be has not been shown here, and would presumably depend upon stratification as well as shear.

Mixed-layer models have been used very successfully to model the vertical transport of momentum in the upper ocean (Kraus and Turner 1967; Niiler 1975; Pollard et al. 1973). Can a simple mixed layer exhibit a spiraling transfer function as observed? The geocentric acceleration in a nonentraining mixed layer is especially simple:

$$A = \frac{\tau_0}{\rho h},$$

where h, the mixed-layer depth, is pure real. At first glance it appears that, since the geocentric acceleration in the mixed layer is always in the direction of the wind stress, there can be no spiral. Indeed, there is never an instantaneous spiral. However, in the average sense of the transfer function, there may be a spiral if the wind stress is coherent with the mixed-layer depth. Such coherence should not be surprising [an example of a spiral in the mean is given by Price et al. (1986)]. The additional effects of momentum transfer across the base of the mixed layer may also permit a spiral. Both D81 and P87 show spirals resulting from slab mixed-layer models in which there is a small momentum flux across the mixed-layer base.

Wind-forced mooring motion has been identified down to at least 1000 m. This bogus response, evident only on surface moorings, is comparable in magnitude to the response in the frictional layer. Mooring motion, with similar phase as in Figs. 3 and 4, was apparent in a positive near-inertial band in D81, although it was considered to be a failure of the statistical analysis (of the relatively short 19-day record) to separate the responses to wind and pressure gradient. A mooring line is evidently very efficient at transporting momentum down from the surface.

The noise in these calculations is due primarily to internal waves. In all frequencies and at all depths, the internal waves are more energetic than both the frictional and mooring motion–induced wind-driven response. The highest coherence was 0.5, observed in the negative near-inertial band at 5 m during LOTUS. Typical coherences in the frictional layer were 0.2 for both frictional and bogus responses. Thus, the magnitude of the wind-driven response was typically 0.2 times the internal wave magnitude, and the ratio of signal to noise energy was 0.04. Long time series were crucial to extracting the signal with any reliability.

The examination of wind driving through the use of geocentric acceleration effectively filters free inertial motions. This improves the signal to noise ratio but precludes any study of the processes of momentum transfer by near-inertial internal waves (Leaman and Sanford 1975). The question of wind driving of free inertial motions requires different techniques than those used here.

REFERENCES

Bendat, J. S., and A. G. Piersol, 1986: *Random Data: Analysis and Measurement Procedures.* Wiley & Sons, 566 pp.

Briscoe, M. G., and R. A. Weller, 1984: Preliminary results from the Long-Term Upper-Ocean Study (LOTUS). *Dyn. Atmos. Oceans,* **8,** 243–265.

Davis, R. E., R. de Szoeke, and P. Niiler, 1981: Variability in the upper ocean during MILE. Part II: Modelling the mixed layer response. *Deep-Sea Res.,* **28,** 1453–1475.

Ekman, V. W., 1905: On the influence of the earth's rotation on ocean currents. *Ark. Mat. Astron. Fys.,* **2,** 52.

Eriksen, C. C., R. A. Weller, D. L. Rudnick, R. T. Pollard, and L. A. Regier, 1991: Ocean frontal variability in the Frontal Air–Sea Interaction Experiment. *J. Geophys. Res.,* **96,** 8569–8591.

Kraus, E. B., and J. S. Turner, 1967: A one-dimensional model of the seasonal thermocline. II: The general theory and its consequences. *J. Atmos. Sci.,* **29,** 11–37.

Large, W. G., and S. Pond, 1981: Open ocean momentum flux measurements in moderate to strong winds. *J. Phys. Oceanogr.,* **11,** 324–336.

Leaman, K. D., and T. B. Sanford, 1975: Vertical energy propagation of inertial waves: A vector spectral analysis of velocity profiles. *J. Geophys. Res.,* **80,** 1975–1978.

Niiler, P. P., 1975: Deepening of the wind-mixed layer. *J. Mar. Res.,* **33,** 405–422.

Philander, S. G. H., 1978: Forced oceanic waves. *Rev. Geophys. Space Phys.,* **16,** 15–46.

Pollard, R. T., P. B. Rhines, and R. O. R. Y. Thompson, 1973: The deepening of the wind-mixed layer. *Geophys. Fluid Dyn.,* **3,** 381–404.

Price, J. F., R. A. Weller, and R. Pinkel, 1986: Diurnal cycling: Observations and models of the upper ocean response to diurnal heating, cooling, and wind mixing. *J. Geophys. Res.,* **91,** 8411–8427.

——, ——, and R. R. Schudlich, 1987: Wind-driven ocean currents and Ekman transport. *Science,* **238,** 1534–1538.

Richman, J. G., R. A. de Szoeke, and R. E. Davis, 1987: Measurements of near-surface shear in the ocean. *J. Geophys. Res.,* **92,** 2851–2858.

Rudnick, D. L., and R. E. Davis, 1988: Mass and heat budgets on the northern California continental shelf. *J. Geophys. Res.,* **93,** 14 013–14 024.

Weller, R. A., 1982: The relation of near-inertial motions observed in the mixed layer during the JASIN (1978) experiment to the local wind stress and to the quasi-geostrophic flow field. *J. Phys. Oceanogr.,* **12,** 1122–1136.

——, D. L. Rudnick, R. E. Payne, J. P. Dean, N. J. Pennington, and R. P. Trask, 1990a: Measuring near-surface meteorology over the ocean from an array of surface moorings in the subtropical convergence zone. *J. Atmos. Oceanic Technol.,* **7,** 85–103.

——, ——, N. J. Pennington, R. P. Trask, and J. R. Valdes, 1990b: Measuring upper ocean variability from an array of surface moorings in the subtropical convergence zone. *J. Atmos. Oceanic Technol.,* **7,** 68–84.

——, ——, C. C. Eriksen, K. L. Polzin, N. S. Oakey, J. W. Toole, R. W. Schmitt, and R. T. Pollard, 1991: Forced ocean response during the Frontal Air–Sea Interaction Experiment. *J. Geophys. Res.,* **96,** 8611–8638.